



Grain growth stagnation in fully dense nanocrystalline Y_2O_3 by spark plasma sintering

Rachel Marder^a, Rachman Chaim^{a,*}, Claude Estournès^b

^a Department of Materials Engineering, Technion – Israel Institute of Technology, 32000 Haifa, Israel

^b CNRS, Institut Carnot Cirimat, F-31602 Toulouse Cedex 9, France

ARTICLE INFO

Article history:

Received 13 July 2009

Received in revised form 14 October 2009

Accepted 3 November 2009

Keywords:

Spark plasma sintering

Nanocrystalline

Grain growth stagnation

Densification

Y_2O_3

ABSTRACT

Nanocrystalline (nc) Y_2O_3 powders with 18 nm crystallite size were sintered using spark plasma sintering (SPS) at 1100 °C and 100 MPa for different durations. Specimens with 98% density and 106 ± 33 nm mean grain size were formed after 20 min. The grain size at the final stage of sintering first increased and then tended to stagnation with the SPS duration. The nanostructure consisted of convex tetrahedron shaped nano-pores at part of the grain boundary junctions. Theoretical calculations were made for grain growth stagnation imposed by either drag from nano-pores at grain junctions or from dense triple junctions; the experimental results were in agreement with grain growth stagnation due to nano-pore drag in nc- Y_2O_3 . The conditions for the stabilization of the nanostructure in Y_2O_3 were determined. Extended SPS duration up to 40 min led to sudden grain coarsening and loss of the nanocrystalline character.

© 2009 Elsevier B.V. All rights reserved.

1. Introduction

Spark plasma sintering (SPS) is a novel hot-pressing technique used for the rapid densification of ceramic powders at temperatures lower than their conventional sintering temperatures [1–5]. Ceramic nano-powders are excellent candidates for densification by SPS due to their large surface area, as the rapid sintering and densification were related to the mass transfer and thermal processes associated with the free surfaces [6–9]. However, at the final stage of sintering, the density of the free surfaces diminishes and the thermal processes are associated with slower kinetics via diffusion along the grain boundaries and in the bulk. Therefore, preservation of the nanostructure character in fully dense ceramics becomes a challenging target due to the inevitable and enhanced grain growth at the final stage of sintering.

SPS has been used recently for rapid fabrication of different fully dense, transparent nanocrystalline or submicrometer grain size oxides [10–15]. Detailed observation of the nanostructure of dense ceramic compacts, after SPS, revealed the presence of isolated nano-pores, mainly located at the grain junctions [11,15]. On one hand, these nano-pores are the main source for the light scattering at the visible and ultraviolet wavelengths thus degrade the optical transparency of polycrystalline ceramics subjected to SPS [10,11,13–15,16]. On the other hand, the closed nano-pores

at the grain boundaries as well as the grain boundary triple junctions (TJ) may act as pinning points which exert drag on the moving grain boundaries, hence lead to grain growth stagnation; this may stabilize the nanocrystalline character of the dense ceramic.

Nanocrystalline 3 mol% yttria stabilized ZrO_2 (3YSZ) powders with 6–8 nm particle size, reached nearly theoretical density when spark plasma sintered at 1180 °C for 9 min with an applied pressure of 40 MPa [17]. In that powder, an increase of the grain size to 70 nm and 250 nm for SPS temperatures of 1100 °C and 1500 °C, respectively, was noted. Nanometric zirconia fully stabilized with 8 mol% yttria (8YSZ) with an initial crystallite size of 21 nm was fabricated by SPS and achieved almost theoretical density at 1200 °C with the holding time of 5 min and the applied pressure 106 MPa [18]. The final grains, about 100 nm in size, preserved their nanocrystalline character. Moreover, it was noted that the applied load had no significant effect on the grain size although it had a large influence on the final density. However, increase in the SPS temperature to 1400 °C clearly enhanced grain growth and resulted in a final grain size of 700 nm. The temperature increase clearly impeded the preservation of the fine nanometric structure. In another study 3YSZ and 8YSZ with an initial particle size of 50 nm were fabricated by two-step sintering approach by applying a lower pressure (106 MPa) at the beginning of the process and higher pressure (141 MPa) once the SPS temperature of 1200 °C was reached [12]. The specimens were successfully densified to over 99% for 17 min; the final crystal size increased only slightly to 55 nm. Moreover, these 8YSZ specimens were transparent, which was related to the

* Corresponding author. Tel.: +972 4 8294589; fax: +972 4 8295677.

E-mail address: rchaim@technion.ac.il (R. Chaim).

elimination of minor amounts of residual pores by the two-step sintering method.

Different strategies may be adopted during the SPS process for preservation of the nanostructure character. Application of high pressures up to 1 GPa for 5 min during SPS of yttria fully stabilized zirconia (Y-FSZ), CeO_2 and Sm-doped CeO_2 nano-powders with ~ 7 nm particles resulted in densities above 98% with average grain size below ~ 20 nm [19]; a critical pressure was found per compound, above which further increase in density may proceed without further grain growth. Following the densification maps for nanocrystalline MgO similar critical pressure was also determined using the HIP model for the SPS [20].

Although pressure increase during the SPS can result in finer grains, grain growth control is the key to stabilization of the nanostructure. The grain growth rate is dictated by the grain boundary mobility and may be lowered by Zener drag where the grain boundaries are pinned by the second phase particles, pores, or other structural features [21,22]. Yet single phase, dense pure nanostructured materials retain high volume fraction not only of grain boundaries but also triple junctions (TJ) and quadruple nodes (QN) [23]. The lower mobility of these structural features may assist limited grain growth or lead to grain growth stagnation in the nanometric materials; this was experimentally observed and theoretically treated in the present paper.

Computer simulations clearly showed the effect of the drag due to second phase particles; grain growth stagnation was possible for large Zener drag, however, small drags led to undesirable abnormal grain growth [24]. Likewise, it was shown by Brook [25] that ultrafine pores may slow down the grain growth kinetics via the grain boundary mobility. For small separation between the pores, grain growth was controlled by the lower mobility of the pores, whereas for large pore separation, abnormal grain growth may take place.

Measurements in bicrystals showed relatively unconstrained mobility of the grain boundaries [26]. However, grain boundary migration in fine-grained materials was found to be highly affected by the rather slow motion of the TJ and thus, significantly lower than calculated for bicrystals. The reduced grain boundary mobility significantly decreased the growth rate; the smaller the average grain size, the larger the reduction in the grain growth rate. Consequently, the TJ drag was believed to be grain size dependent [27]. Grain growth stagnation became feasible for ultrafine structures. Due to the reduced grain boundary mobility, the conventional parabolic grain growth kinetics was found to change into linear behavior at the initial stages of growth for fine enough grains, which notably lowered the evolution rate. The TJ drag, determined by the grain boundary as well as the TJ mobility, was shown to slow down the grain growth for any n -sided grain [28]. Moreover, under a certain critical number of sides, the grains become locked and grain growth cannot occur. The TJ drag was found not only to reduce the grain growth rate but also change the final grain size distribution. Chokshi modeled the criteria under which the grain growth was constricted by the TJ and showed the importance of the TJ drag especially for nanocrystalline ceramics [29]. The experimental results from different nanocrystalline systems exhibited similar behavior, where the rapid initial grain growth tends to stagnate [30–35]; afterwards discontinuous grain growth may be observed.

Cubic yttria (Y_2O_3) is an appropriate oxide used as a model system for investigation of the nanostructure stabilization. In this respect, nanocrystalline Y_2O_3 (nc- Y_2O_3) was sintered by pressureless sintering [36], two-step sintering [37], and SPS [38,39]. However, densities up to 97% with 500 nm mean grain size were formed by the SPS at 850°C [38]. Densification and grain growth may become competitive processes with the change in the SPS process parameters. This effect was clearly observed in nc- Y_2O_3 subjected to SPS under 100 MPa for 5 min at different temperatures [39]. The grain growth rate above 1400°C dominated over

the densification rate, thus led to entrapped pores within the grains resulting in lower final densities. It was concluded that an optimal SPS temperature exists above which fully dense ceramics may not be practically accessible [39]. Appropriate SPS at the lower temperature of 1100°C for extended durations successfully preserved the nanometric size of the grains, albeit with some isolated pores at the grain corners, as will be shown here. With respect to the theoretical expectations, the present work attempts to address the question whether and under which conditions the isolated nano-pores and the triple junctions can stabilize the nanocrystalline character via grain growth stagnation in Y_2O_3 . Well developed sintering and densification models were modified and used to compare the theoretical predictions for the grain growth evolution at the final stage sintering in nanocrystalline Y_2O_3 compacts to the experimental results.

2. Experimental

Nanocrystalline Y_2O_3 powder (Cathay Advanced Materials, China) with 99.99% purity and 18 nm mean crystallite size (diameter) was used. Discs of 8 mm in diameter and 2 mm thick were fabricated using the SPS unit (Dr. Sinter, SPS 2080) of the Plateforme Nationale de Frittage Flash (PNF2) du CNRS located at Toulouse. The as-received powders were pressed within the graphite die and isolated by graphite foils from the die wall and the punch surfaces. The SPS was performed at 1100°C using the heating rate of $180^\circ\text{C min}^{-1}$ and the pulse duration of 3.3 ms and sequence 12–2 (on–off). The temperature was raised to 600°C over a period of 3 min, and from that point it was monitored by the optical pyrometer. Uniaxial pressure of 100 MPa was applied at 1100°C for various durations (5–40 min). The vacuum level of 2–3 Pa was constant during the SPS process. Different SPS parameters such as temperature, pressure, time, ram displacement and its rate were continuously recorded.

The sintered density was measured by the Archimedes method according to the ASTM standard C 20–92 ($\pm 0.5\%$ accuracy). The theoretical density 5.030 g cm^{-3} was used. The crystal structure was characterized using X-ray diffraction (Philips PW 3710). For the scanning electron microscopy (SEM) observations, the sintered specimens were prepared by mechanical polishing with diamond pastes down to $0.5\text{ }\mu\text{m}$, and thermal etching at 1000°C for 20 min. The microstructure of the sintered specimens was characterized using high resolution SEM (HRSEM, Leo Gemini 982, operated at 4 kV). About 250 grains were counted in each specimen for the grain size statistics, using the largest axis of the grain from HRSEM images. The specimens for transmission electron microscopy (TEM, FEI Tecnai G² T20, operated at 200 kV) observations were prepared by conventional mechanical and ion milling to electron perforation.

3. Results

3.1. Densification

The as-received powder was characterized in a previous work [39]. XRD examination of the sintered specimens showed that the cubic crystal structure of the nanocrystalline powder was retained in all the specimens. The ram displacement, temperature and pressure during the SPS cycle were recorded and used with the specimen mass and dimensions for determining the linear shrinkage versus time. A few percents of linear shrinkage took place immediate to the heating burst to 600°C (Fig. 1) probably due to some grains rearrangement. No pressure was applied until the SPS temperature was reached. However, the main shrinkage always started during the heating-up stage around 800°C (without pressure) and increased further with the pressure application at the SPS temperature (1100°C). The desired pressure of 100 MPa is reached

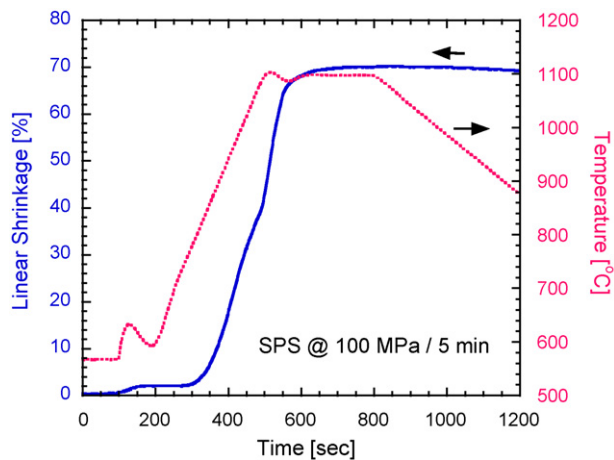


Fig. 1. Linear shrinkage versus SPS temperature for 5 min. The shrinkage starts around 800 °C, accelerates when the pressure is applied at 1100 °C and ends within 3 min at the SPS temperature.

within ~90 s from the moment of its application. The linear shrinkage versus temperature prior to the pressure application followed a sigmoid shape curve. The maximal shrinkage rate calculated at the inflection point of the sigmoid was $\sim 2.5 \times 10^{-3} \text{ [s}^{-1}]$ following the dimensional changes of the specimen with time. Application of 100 MPa pressure resulted in a constant shrinkage rate (between 500 s and 550 s in Fig. 1) in the order of $\sim 10^{-2} \text{ [s}^{-1}]$ irrespective of the SPS duration. The linear shrinkage during the heating and at 1100 °C constituted each ~50% of the total shrinkage and took place during 200 s. Once the SPS pressure was applied the linear shrinkage tended to saturate after ~3 min at the SPS temperature. The higher densification rate under the applied pressure may be an indicative of the very fast densification mechanism at this stage.

The relative density and the corresponding mean grain size versus the SPS duration are shown in Fig. 2. The specimens sintered at 1100 °C exhibited decreasing densification rate with the SPS duration. The density measured by the Archimedes method increased from 93.6% to 98.8% which is comparable to porosities between ~6% and 1%, respectively. The grain size first increased with time but tended to saturation around 105 nm while discontinuous grain growth was observed at the longer SPS duration of 40 min.

HRSEM images from the different sintered specimens revealed dense and homogeneous nanostructure with equiaxed grains (Fig. 3). All the specimens exhibited log-normal grain size distribution with standard deviations between 30% and 40% of the mean grain size. Significant grain coarsening was observed for 40 min SPS

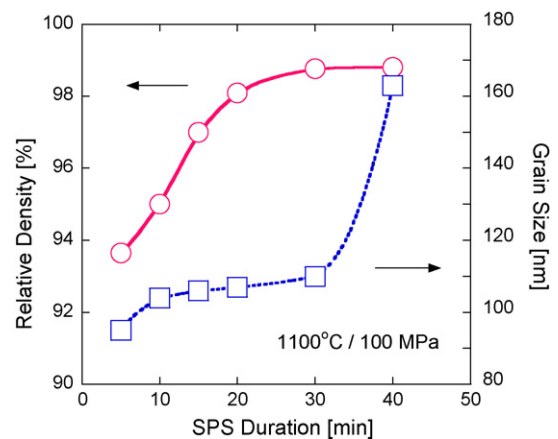


Fig. 2. Relative density and grain size of nanocrystalline Y_2O_3 versus SPS duration at 1100 °C and 100 MPa.

duration (Fig. 3b) where elongated-shape grains were also visible. TEM images showed the interior of the dense equiaxed nano-grains to be dislocation-free (Fig. 4). Nevertheless, many grain boundaries were characterized by the networks of dislocations, implying low angle grain boundaries (arrowed in Fig. 4b). TEM images revealed high density of grain corners either dense or containing nano-size pores (Fig. 4a); their exact locations were confirmed by tilting experiments. The radius of the visible nano-pores ranged between 5 nm and 28 nm using TEM images; smaller pores may also be present, albeit unresolved. The observed pore diameter was always much smaller than the mean grain size in the corresponding specimens. The coordination number of the observed nano-pores varied between 4 and 9 in two dimensional cross-sections in SEM. The nano-pores coordination number from the TEM images was found to be between 3 and 5 (in two dimensional image of the projected volume). However, it should be noted that TEM observations clearly distinguish the true nano-pores while large coordinated pores in SEM may origin from detached grains caused by the specimen preparation.

3.2. Grain growth stagnation

During the densification no or very limited plastic deformation is expected, the yield stress for ultrafine grain sized Y_2O_3 at 1100 °C [39,40] is higher by 2–3 folds than the present SPS applied pressure. This is in agreement with the dislocation-free nanostructure observed in the specimens. In addition, no plastic deformation was observed during compression tests of similar specimens at 800 °C

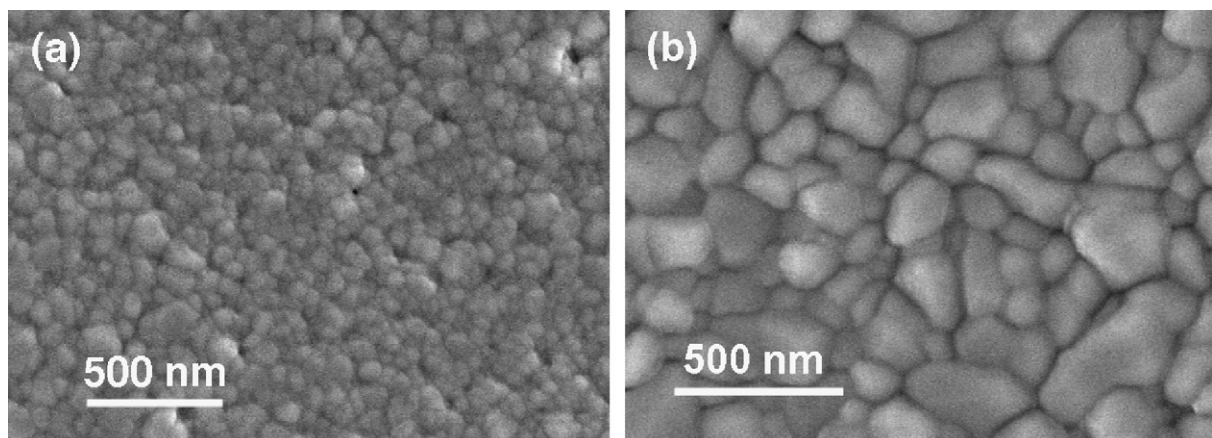


Fig. 3. HRSEM images from nc- Y_2O_3 after SPS at 1100 °C and 100 MPa for (a) 5 min and (b) 40 min durations.

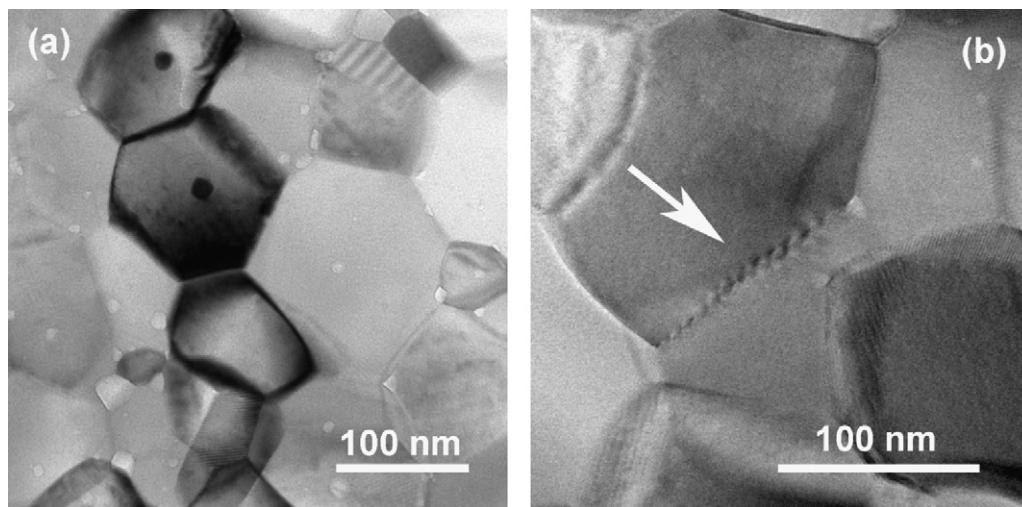


Fig. 4. Bright field TEM images from nc-Y₂O₃ after SPS at 1100 °C and 100 MPa for (a) 10 min showing dense grain boundary corners as well as containing nano-pores. (b) 40 min showing low angle grain boundary (arrowed) typical of the nanostructure.

under 375 MPa or at 900 °C under 135 MPa, which confirmed the lack of dislocation activity at these temperatures [41]. On the other hand, the high strain rates calculated are in agreement with rapid densification by grains sliding over each other and grain rotation, both aided by enhanced surface diffusion [39]. Following the grain size evolution in nanocrystalline Y₂O₃ powders versus temperature [42] some particle coarsening is also expected during the heating-up. Moreover, a densification to above 90% density was recorded at the point the pressure of 100 MPa was reached. Therefore, from that point, the isothermal SPS densification at 1100 °C should be related to the final stage of sintering, where internally dense nano-grains, with isolated pores located at their junctions, are present.

In addition, as was noted by Raj and Lange [43] if the strain rate during the deformation/densification is low enough it may allow time for the diffusional processes needed for the grain boundary migration, hence grain growth. The critical strain rate below which the grains remain equiaxed due to the TJ drag was expressed in their equation as:

$$\dot{\epsilon}_c = 2 \cdot 10^{-2} \frac{\Omega^{1/3}}{G^2} \frac{\gamma_{gb}}{kT} \delta_{gb} D_{gb}^{\perp} \quad (1)$$

where γ_{gb} is the grain boundary energy, Ω is the atomic volume of the diffusing species, G is the grain size (diameter), δ_{gb} is the grain boundary thickness, D_{gb}^{\perp} is the grain boundary diffusion coefficient of the slowest ionic species (Y³⁺) *perpendicular* to the gb, k is the Boltzmann's constant, and T is the absolute temperature.

Considering conservative treatment where neglecting the growth of the Y₂O₃ particles during the heating [42,44] and using the following values for Y₂O₃: $\Omega = 7.45 \times 10^{-29} [\text{m}^3 \text{atom}^{-1}]$, $\gamma_{gb} \approx 0.83 [\text{J m}^{-2}]$ [45], and $\delta_{gb} D_{gb}^{\perp} = 2.38 \cdot 10^{-12} [\text{m}^3 \text{s}^{-1}] \cdot \exp(-410 [\text{kJ mol}^{-1}]/RT)$ determined from the *gb mobility tests* [46], the strain rates $1.2 \times 10^{-9} [\text{s}^{-1}]$, $5.6 \times 10^{-6} [\text{s}^{-1}]$ and $2.2 \times 10^{-3} [\text{s}^{-1}]$ were calculated for 20 nm grains at 700 °C, 900 °C, and 1100 °C, respectively. These strain rates are still lower by one to three orders of magnitudes compared to the strain rates measured during the heating-up and at 1100 °C by SPS. Consequently, the rapid grain growth during the heating-up should be related to mechanisms with faster kinetics than normal grain growth, such as grain sliding and rotation [47,48]. Analysis by Cahn and Taylor [48] has shown that grains sliding over each other can lead to grain rotation. The grain reorientation can be followed by growth of the larger grains at the expense of the smaller grains leading to grain coalescence. The rapid increase in the observed grain size at 5 min

SPS at 1100 °C, from the original crystallite size of the powder, can be related to such grain coalescence. The widespread low angle grain boundaries observed in the present nanocrystalline Y₂O₃ specimens may be indicative of such rotations, where sliding grains reorient to lower the interfacial energy [48]. The measured strain rates during densification are compatible with nano-grains sliding over each other and assisted by surface diffusion. Further densification at the SPS isotherm, albeit slow, proceeds during the grain stagnation, most probably by grain boundary diffusion.

The observed nanostructures, prior to the sudden grain coarsening at 40 min SPS, consisted of grains in the range 50–150 nm in diameter and convex tetrahedron shaped pores with radii between 5 nm and 28 nm, located at the grain junctions. A few larger pores of the order of the grain size were present and believed to originate from the local non-homogeneity in the green density and will be ignored. Assuming the critical dihedral angle at the junction (where grain boundary intersects the pore surface) to be 120°, the critical coordination number for pore stability is 9 in 3D (space) and 6–7 for 2D (in plane) [49]. Consequently, the observed nano-pores with coordination numbers lower than 6 or 7 may be annihilated during sintering, while those with higher coordination numbers may be stable and even grow. The observed nano-pores are much smaller than the average grain size hence assure low pore coordination number (3 or 4) and may be annihilated. This may take place by diffusion of atoms from the grain boundaries and of vacancies from the pores through the grain boundaries as the fastest paths to the specimen external surfaces. Since the nano-pores were not all-around present, the grain growth stagnation should be treated not only in terms of nano-pore drag but also in terms of triple junction drag mechanism. The high density of grain triple junctions with lower mobilities than the grain boundaries may impose drag to the grains mobility, which may assist to the grain growth stagnation [29,43,50].

4. Theoretical calculations

Regardless of the mechanism by which the powder compact is densified during the second stage of sintering, the final stage, when isolated pores form, takes place by diffusional processes. As was indicated by Rahaman [51] isolated pores at the grain boundaries may control the grain growth via three different transport mechanisms of surface diffusion, lattice diffusion and evaporation/condensation through a vapor phase. The vapor pressure often increases with the temperature increase hence mass transfer by

evaporation–condensation may become important only at very high sintering temperatures. Lattice diffusion is also effective only at the highest sintering temperatures. Nevertheless, due to the short characteristic diffusion distances in the nanocrystalline materials, this mechanism may also be active. The fastest atomic transport mechanisms which dominate at the lower sintering temperatures are thus surface and grain boundary diffusion.

The observed stagnation in the grain growth can be related both to the pinning effect imposed by the grain boundary junctions (TJ and QN) as well as to drag by the nano-pores at the grain corners. These aspects will be considered below from the theoretical point of view and the calculated results will be compared to the experimental observations.

4.1. Triple junction drag

Several models were developed in the literature for evaluating the conditions for grain growth stagnation via triple junction and quadruple node drag [25–29]. Following the approach by Raj and Lange [43], Chokshi [29] derived the following equation for estimation of the temperature–time conditions at which the triple junctions impose drag which stabilizes the nano-size character against grain growth:

$$z^2 = \frac{4\gamma_{gb}\Omega^{1/3}}{kT} \delta_{gb} D_{gb}^\perp \cdot t \quad (2)$$

where t is the time, and the term z represents the displacement of the triple junction from its equilibrium state, where the dihedral angles retained their equilibrium value. TJ drag leads to non-equilibrium dihedral angles [43]. However, for small displacements the equilibrium dihedral angles can be maintained and in that case the TJ does not impose drag on the grain boundary. The condition $z \geq 0.01G$, where G is the average grain diameter, was chosen as a reasonable estimate for retaining the dihedral angle to its equilibrium value [29,43]. The triple junction displacement–grain size dependence, may be derived more accurately by a simple momentary energy balance in one dimension. The triple junction displacement may impose elastic energy which can be balanced by the energy due to the grain boundary line tension at the triple junction:

$$\frac{E(2z/G)^2}{2} = \frac{\gamma_{gb}}{(G/2)} \quad (3)$$

where E is the elastic modulus at the corresponding temperature.

Assuming isotropic elasticity, the three-dimensional version of Eq. (3) contains a factor of 1.5 in the term at the right hand side of the equation. However, in order to be consistent with Chokshi's approach, the one-dimensional version of Eq. (3) will be used in our treatment. For TJ displacements higher than a critical value, TJ migrates via mass transfer.

The imposed displacement of the triple junction in Eq. (3) is both grain size and temperature dependent. It converges to the value of $0.01G$ [29] at the grain diameter above 150 [nm]. Combining Eqs. (2) and (3) the critical grain size below which the TJ drag is effective is given by:

$$G \leq \frac{4E\Omega^{1/3}\delta_{gb}D_{gb}^\perp t}{kT} \quad (4)$$

Following Chokshi [29] the master curve for all temperatures may be plotted using the form:

$$G \leq \frac{4E\Omega^{1/3}}{k} (\Theta) \quad (5)$$

where $\Theta = \delta_{gb}D_{gb}^\perp t/T$ is the temperature-compensated time parameter.

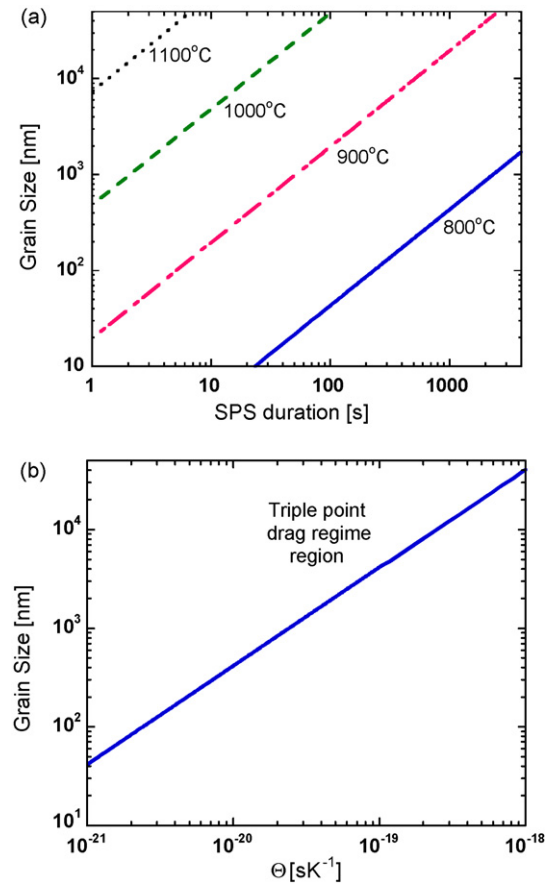


Fig. 5. (a) Grain size–duration–temperature conditions for triple junction limited grain growth in nc-Y₂O₃. At a given grain size, the TJ drag holds for durations to the left of the isothermal lines. (b) Master curve of the same data in (a) where combinations of temperature–time can be derived.

Using the previous data for Y₂O₃ together with the temperature dependent elastic modulus [52], the Eqs. (4) and (5) were calculated and plotted (Fig. 5a and b, respectively) to reveal the conditions for grain growth stagnation by the TJ drag. It should be noted that the number density of the triple junctions decreases very fast with increase in the grain size, hence, TJ contribution to grain size stabilization diminishes rapidly with time.

The isotherms in Fig. 5a present the corresponding SPS durations for which further growth of grains with a given size, may efficiently be inhibited by the triple junction drag. As an example, the 100 nm grain size in dense Y₂O₃ can be maintained only for 5 s at 900 °C, or for 230 s at 800 °C, before further growth. Grains with this size will grow almost immediately when reaching 1000 °C. For comparison, grain growth stagnation around 105 nm was found up to 30 min SPS duration at 1100 °C. The calculated results in Fig. 5 are not in agreement with the experimental findings. The uncertainties in the diffusion coefficient and activation energy are too small to cause the shift of the observed experimental data to the higher temperatures compared to the theoretical results. Nevertheless, the presence of the nano-pores may have a more dominating effect on grain growth stagnation as will be discussed below.

Following Fig. 5 it can be seen that for a given SPS duration, TJ drag may hold for large grains, but it is not effective for small grains. However, the number density of the TJ's become negligible for large grains. Lowering the SPS temperature increases the TJ drag effect for finer grains, albeit it also reduces the rate of the diffusional processes necessary for full densification.

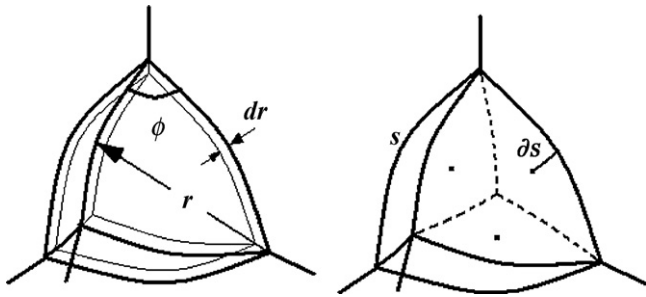


Fig. 6. Reuleaux tetrahedron shaped pore with radius r , dihedral angle ϕ , and surface area A , shrinks in a self-similar way by Δr . The pore surface can be divided into 12 triangles (3 are shown by dashed lines for the upper face), with ∂s arc between their center of mass to the closest grain boundary with length s .

4.2. Pore drag

The present observed nanostructure consisted equiaxed polyhedron shaped nano-grains of 50–150 nm in diameter and convex Reuleaux tetrahedron shaped nano-pores with 5–28 nm in radius (see Figs. 4 and 6) located at the grain corners. The observed grain size evolution at 1100 °C was in agreement with grain growth stagnation followed by discontinuous grain growth. However, albeit slow, densification proceeded during the grain stagnation. In this respect, two processes of pore shrinkage and pore coalescence with competing mechanisms should be considered. Since densification to above 90% density was already recorded at the moment the SPS pressure of 100 MPa is reached, the isothermal SPS densification at 1100 °C should be related to the state of final stage sintering. This may take place by diffusion of atoms from the grain boundaries and of vacancies from the pores, both through the grain boundaries as the fastest paths to the specimen external surfaces. Therefore, pore shrinkage (hence densification) is controlled by the grain boundary diffusion.

On the other hand, pore coalescence (and grain growth) occurs by migration of the grain boundaries and pores. Nevertheless, due to the drag imposed by the pores on the grain boundaries, the gb migration is controlled by the pore mobility, hence, by surface diffusion at the pore surfaces. This is true as long as the pores are attached to the grain boundaries.

The total change in pore size during the sintering can be described by the following relation [53]:

$$\frac{dr}{dt} = \left(\frac{dr}{dt}\right)_G + \left(\frac{dr}{dt}\right)_\rho \quad (6)$$

The first term describes the rate of pore shrinkage at constant grain size, where the second term describes the rate of pore coarsening at constant relative density. Assuming the pore shrinkage and coarsening at the final stage sintering to be controlled by grain boundary and surface diffusion mechanisms, respectively, the kinetics of the two processes can be compared. Several models were developed in the literature in order to evaluate the conditions for pore coarsening, drag or shrinkage [25,54]. We assume grains with Tetrakaidecahedron (TKDH) shape with caliper diameter G , consisting of convex tetrahedron shaped pores with radius r , located at all grain corners [55]. The pore shrinkage rate for this model at constant grain size is given by (see Appendix A):

$$\left(\frac{dr}{dt}\right)_G = \frac{24(\sqrt{2}-1)\Omega D_{gb}\delta_{gb}}{(\pi-\sqrt{3})r^2 kT} \left(\frac{\gamma_{sv}}{r} + \frac{P_a}{\rho}\right) \quad (7)$$

where D_{gb} is the diffusion coefficient of the slowest ionic species (Y^{+3}) along the grain boundaries, γ_{sv} is the solid–vapor surface energy, P_a is the applied SPS pressure, and ρ is the relative density.

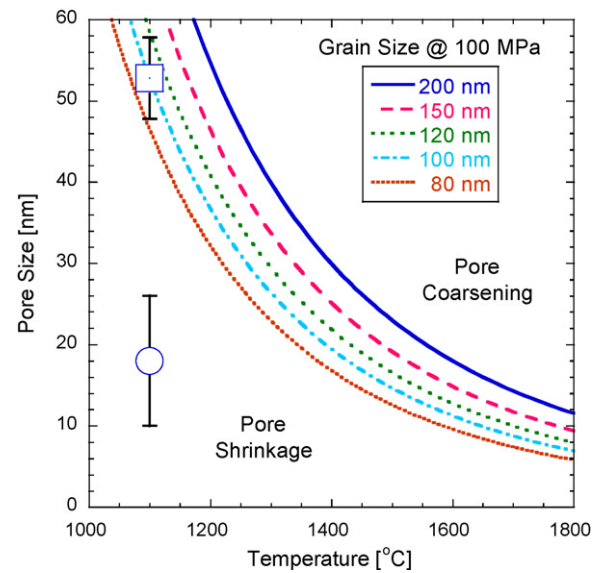


Fig. 7. Pore size–temperature at constant grain size and 100 MPa pressure, showing the conditions for pore limited grain growth in nc- Y_2O_3 . The lines represent the loci of critical pore radius versus temperature below which the nano-pores exert drag on the grain boundaries leading to grain growth stagnation. The experimental pore size and grain size were shown by the open circle and square, respectively, for which grain growth stagnation was observed.

The corresponding rate for pore coarsening was also developed as (see Appendix A):

$$\left(\frac{dr}{dt}\right)_\rho = \frac{1.2\Omega\gamma_{gb} D_s \delta_s}{28.6} \frac{G}{kT} \frac{1}{r^4} (17.9 - 6.2\phi) \quad (8)$$

where D_s is the diffusion coefficient of the slowest ionic specie (Y^{+3}) at the pore surface, δ_s is the depth at which surface diffusion is effective, and ϕ is the pore dihedral angle.

Using the previous data and the following values for Y_2O_3 : $\delta_{gb} = 10^{-9}$ [m], $\delta_s = 2 \times 10^{-9}$ [m], $\rho = 0.94$, $\gamma_{sv} \approx 1.66$ [J m $^{-2}$] [45], $\phi = 2\pi/3$, $D_s = 2.41 \times 10^{-8}$ [m 2 s $^{-1}$] $\times \exp(-184$ [kJ mol $^{-1}$]/ RT) [56], and $D_{gb} = 1.65 \times 10^{-6}$ [m 2 s $^{-1}$] $\times \exp(-290$ [kJ mol $^{-1}$]/ RT) determined from the sintering tests [57], the rate of these two competing processes were calculated. By equating Eqs. (7) and (8), the pore size as a function of temperature and grain size can be evaluated. The results were plotted in terms of pore size versus temperature at constant grain size as shown in Fig. 7. At a given temperature and grain size, a critical pore size is determined below which the pores are attached to the gb and can effectively drag it and lead to grain growth stagnation (denoted as ‘pore shrinkage’ region in Fig. 7). As an example, at 1100 °C and 100 nm grain size, the critical pore size is 53 nm (open square in Fig. 7); pores smaller than ~53 nm can lead to grain growth stagnation. This is in good agreement with the experimental findings where stagnated grain growth was observed for 106 nm grains with 28 nm and smaller pores (open circle in Fig. 7). It should be noted, that at a given relative density, the volume fraction of the nano-pores is well determined. The smaller the average pore size, the higher the number density of the nano-pores at the grain junctions, hence, grain growth stagnation is more effective. Therefore, according to the theoretical findings, stagnation of grain growth in nc- Y_2O_3 sintered at 1100 °C is principally controlled by the drag from porous grain junctions rather than drag due to the dense TJ’s.

The effectiveness of the pore drag in grain growth stagnation was also related to the pore–grain edge interactions, especially for very small grains (~100 nm) [21]. Grain growth in dense nanocrystalline materials may occur also by grain rotation [47,48] in addition to grain boundary migration. Many pores located at the grain

corners of a given grain can pin its rotation and lead to grain growth stagnation. Therefore, a critical pore volume fraction exists below which grain growth stagnation may be lost.

At high temperatures, the critical pore size becomes smaller and the possibility for grain growth stagnation due to pore drag diminishes. At these temperatures, pore coalescence becomes important and thus grain growth can take place. In the lower temperature region, the critical pore size is large enough, so that pore shrinkage becomes the sole mechanism. However, low temperatures are associated with slower diffusion kinetics, lower grain boundary mobility and thus, result in reduced final density. Pore size control is crucial; theoretically large enough pores can drag the grain boundary at the lower temperatures. Nevertheless, large pores can be detached from the grain boundaries provided the grain boundary mobility is high enough. Such pores will not inhibit grain growth but remain as residual porosity. In this respect, the sintering temperature is critical and should be chosen carefully for the growth stagnation to dominate. The 2D Monte Carlo simulations have shown the major effect of the initial pore size on the microstructure evolution: smaller pore size resulted in smaller grain size [58]. A parabolic grain growth was observed when the porosity decreased below 3%. The rapid grain growth in the present nc-Y₂O₃ occurred after the grain growth stagnation, at ~1.2% porosity, in agreement with the theoretical expectations.

Finally, computer simulations of grain growth at the final stage sintering by Hassold et al. [54] have shown that too rapid pore shrinkage hampered obtainment of the equilibrium pore shape that, in turn, decreased the effectiveness of the pore drag. Following Eq. (7) the pore drag effectiveness may be controlled via the SPS applied pressure. Therefore, decrease in the SPS temperature and increase in the SPS pressure are expected to retard grain growth.

5. Overall view

Grain growth in nanocrystalline materials was found to follow a linear law prior to the normal parabolic character. Estrin et al. [59,60] explained this reduced (linear) grain growth in terms of the free volume present at the grain boundaries. The vacancies associated with this free volume at the grain boundaries diffuse into the crystal, increase its vacancy concentration and thus its free energy. This, in turn, opposes the reduction in the free energy, hence reduces the overall driving force for grain growth. Above a threshold or critical grain size value, the grain growth passes from a linear to parabolic behavior [61]. The loss of the free volume is also temperature dependent and discontinuous nano-grain growth can also take place at a critical temperature [35]. The densification diffusional processes at the SPS temperature exhaust the free volume and decrease the volume fraction of the nano-pores at the grain boundaries with time. The interrupted grain growth stagnation observed after 40 min of SPS is the manifestation of this behavior, and is in agreement to the theoretical expectations. Consequently, fully dense nanostructured Y₂O₃ with grain size below ~100 nm may be preserved by SPS at temperature below 1100 °C provided longer term SPS schedule.

6. Summary

The observed grain growth stagnation in nanocrystalline Y₂O₃ was investigated with respect to two possible drag mechanisms: triple junction drag and nano-pore drag. The theoretical approach for triple junction drag developed by Raj and Lange and later extended by Chokshi, based on non-equilibrium dihedral angle at the triple junction was refined. The present calculations showed that triple junction drag in nanocrystalline Y₂O₃ is not significant at relatively low sintering temperatures and unrealistic at high temperatures.

Grain growth stagnation was attributed to the presence of nano-pores at grain junctions. The SPS process resulted in almost fully dense specimens with nano-pores at the grain junctions. A refined model for pore densification and coalescence based on grain boundary diffusion for pore shrinkage and surface diffusion for grain growth was used to determine the critical pore size necessary for grain growth stagnation. The theoretical expectations were in good agreement with the experimental results. Nano-pores were beneficial for stabilizing the ceramic nanostructure, but may be undesirable when manufacturing theoretically dense ceramics. Grain growth stagnation ceased at long SPS durations resulting in rapid grain growth and loss of the nanocrystalline character.

Acknowledgments

The financial support of the Israel Ministry of Science and the Fund for Promotion of Research at the Technion are gratefully acknowledged. The authors thank G. Raimbeaux and G. Chevallier from CIRIMAT for the help in the SPS experiments.

Appendix A.

Following the general approach by Handwerker et al. [53] the simultaneous densification and grain growth at the final stage of sintering may be expressed by two terms describing the change in the pore size by these processes:

$$\frac{dr}{dt} = \left(\frac{dr}{dt}\right)_G + \left(\frac{dr}{dt}\right)_\rho \quad (A1)$$

The first term describes the rate of pore shrinkage at constant grain size, where the second term describes the rate of pore coarsening at constant relative density. Since such coarsening is associated with grain growth and pore coalescence, it is related to grain growth by [53]:

$$\left(\frac{dr}{dt}\right)_\rho = \frac{r}{G} \frac{dG}{dt} \quad (A2)$$

Comparison of the two process rates can give sufficient information about the conditions at which pores can control grain growth.

A.1. Pore shrinkage

The densification rate is assumed to be directly related to the shrinkage rate of the pores. The densification rate for the Tetrakaidecahedron (TKDH) grains with spherical pores located at corners of the grains was first developed by Coble [62,63] assuming lattice diffusion. This model was revised by Kang [64] to take account for the grain boundary diffusion. Following these models, let assume that Reuleaux tetrahedron shaped pores with radius r shrink in a self-similar way [55] as shown in Fig. 6. The pore surface area, A for this shape with apex (dihedral) angles of 120° is given by [55]:

$$A = \frac{r^2}{2} (\pi - \sqrt{3}) \quad (A3)$$

The amount of vacancies with volume equal to Adr (Fig. 6a) is removed from the shell of the pore surface with radius r and thickness dr . This amount should flow during time dt through the cross-section area of six grain boundary arcs, each with length s , and gb thickness δ_{gb} , that cross the pore surfaces. The relation between the pore radius and the arc length for the Reuleaux tetrahedron is given by:

$$s = r\sqrt{2} \quad (A4)$$

The diffusion flow equation for this problem can be expressed by:

$$-D_{gb} \frac{\partial c}{\partial x} = \frac{A}{6s\delta_{gb}} \left(\frac{dr}{dt} \right)_G \quad (A5)$$

The concentration gradient acting as a driving force for diffusion in a pure material is due to the curvature difference between the pore and the grain boundary (or the external surfaces). Since the pore surface is convex, vacancies from any location of the surface can diffuse to their nearest grain boundary. The average distance that vacancies pass from the pore surface to the nearest gb's can be considered as the distance, $\partial s = \partial s$, over which the vacancy gradient exists. The distance ∂s is equal to the arc length between the center of mass of each of the 12 cup shaped triangles (three of which are shown in Fig. 6b) which comprise the total pore surface, and symmetrically located with their closest gb. The length of ∂s is related to the pore radius by:

$$\partial s = r \left(1 - \frac{\sqrt{2}}{2} \right) \quad (A6)$$

Assuming planar grain boundaries, the concentration gradient is given by:

$$\frac{\partial c}{\partial s} = \frac{2\Omega\gamma_{sv}}{kTr} \frac{1}{r(1-\sqrt{2}/2)} \quad (A7)$$

Substituting from Eqs. (A3), (A4) (A6) and (A7) into (A5) one derives the shrinkage rate of the convex tetrahedron shaped pores as:

$$\left(\frac{dr}{dt} \right)_G = \frac{24(\sqrt{2}-1)}{(\pi-\sqrt{3})} \frac{\Omega\gamma_{sv}D_{gb}\delta_{gb}}{kTr^3} \quad (A8)$$

Here γ_{sv} is the solid-vapor surface energy, Ω is the atomic volume of the rate controlling diffusing ion, k is the Boltzmann's constant, and T is the absolute temperature.

The applied SPS pressure P_a is an additional driving force for the pore shrinkage that should be accounted. Therefore, the *maximal pore shrinkage rate* is given by:

$$\left(\frac{dr}{dt} \right)_G = \frac{24(\sqrt{2}-1)}{(\pi-\sqrt{3})} \frac{\Omega}{r^2} \frac{D_{gb}\delta_{gb}}{kT} \left(\frac{\gamma_{sv}}{r} + \frac{P_a}{\rho} \right) \quad (A9)$$

where ρ is the relative density at the final stage of sintering (i.e. $\rho \geq 0.92$).

A.2. Pore coarsening

Coarsening of the isolated pores is associated with grain growth. Let us assume that the observed grain growth stagnation is due to the pinning effect of these pores, and the pore mobility is controlled by surface diffusion within the pores. The coarsening rate for several pore configurations was modeled [65–68] assuming all pores always attached to, and dragged by the gb's. The grain growth rate controlled by moving polyhedral pores can be expressed by [66]:

$$\frac{dG}{dt} = \frac{F_b}{N_A} \left[\frac{D_s\delta_s\Omega}{kTr^4} (17.9 - 6.2\phi) \right] \quad (A10)$$

where F_b is the driving force acting on the grain boundary, N_A is the number of the pores per gb unit area, D_s is the surface diffusion coefficient of the slower diffusing specie, δ_s is the depth from the pore surface within which surface diffusion is effective, and ϕ is the dihedral angle at the pore apices (i.e. 120°). The right hand term in the square parenthesis in Eq. (A10) presents the pore mobility.

The driving force acting on the grain boundary is due to the gb curvature and is given by:

$$F_b = \frac{\alpha\gamma_{gb}}{G} \quad (A11)$$

where G is the mean caliper diameter of the TKDH grain, γ_{gb} is the gb energy, and α is the gb geometric factor ($\alpha = 1.2$).

The number of the pores (regardless of their shape) per unit area of the TKDH grain boundary is related to the number of the pores per unit volume, N_V , by [69]:

$$N_A = 2rN_V \quad (A12)$$

The TKDH grain has 24 corners (pores) each shared by 4 grains. Therefore, the number of pores per unit volume is given by:

$$N_V = \frac{6}{V_{TKDH}} \quad (A13)$$

where V_{TKDH} is the grain volume. Substituting the appropriate volume for the TKDH grains [70] leads to:

$$N_A = 28.6 \frac{r}{G^3} \quad (A14)$$

Substituting the corresponding parameters from Eqs. (A11) and (A14) into (A10) the grain growth rate is given as:

$$\frac{dG}{dt} = \frac{1.2\Omega\gamma_{gb}}{28.6} \frac{D_s\delta_s}{kT} \frac{G^2}{r^5} (17.9 - 6.2\phi) \quad (A15)$$

Substituting (A15) into (A2) the pore coarsening rate is given by:

$$\left(\frac{dr}{dt} \right)_\rho = \frac{1.2\Omega\gamma_{gb}}{28.6} \frac{D_s\delta_s}{kT} \frac{G}{r^4} (17.9 - 6.2\phi) \quad (A16)$$

The two rates of pore shrinkage (Eq. (A9)) and pore coarsening (Eq. (A16)) can be compared versus grain size, pore size, and temperature to reveal the conditions at which pores can cause grain growth stagnation or be eliminated.

References

- [1] Z.A. Munir, U. Anselmi-Tamburini, M. Ohyanagi, J. Mater. Sci. 41 (2006) 763–777.
- [2] M. Nygren, Z. Shen, Key Eng. Mater. 264–268 (2004) 719–724.
- [3] M. Yoshimura, T. Ohji, M. Sando, K. Niihara, J. Mater. Sci. Lett. 17 (1988) 1389–1391.
- [4] R.S. Mishra, A.K. Mukherjee, Mater. Sci. Eng. A 287 (2000) 178–182.
- [5] R. Chaim, M. Levin, A. Shlayer, C. Estournes, Adv. Appl. Ceramics 107 (2008) 159–169.
- [6] M. Tokita, New Ceram. 10 (1997) 43–53 (in Japanese).
- [7] J.R. Groza, M. Garcia, J.A. Schneider, J. Mater. Res. 16 (2001) 286–292.
- [8] V. Mamedov, Powder Metall. 45 (2002) 322–328.
- [9] R. Chaim, Mater. Sci. Eng. A 443 (2007) 25–32.
- [10] R. Chaim, Z. Shen, M. Nygren, J. Mater. Res. 19 (2006) 2527–2531.
- [11] U. Anselmi-Tamburini, J.N. Woolman, Z.A. Munir, Adv. Funct. Mater. 17 (2007) 3267–3273.
- [12] S.R. Casolco, J. Xu, J.E. Garay, Scripta Mater. 58 (2008) 516–519.
- [13] K. Morita, B.N. Kim, K. Hiraga, H. Yoshida, Scripta Mater. 58 (2008) 1114–1117.
- [14] G. Bernard-Granger, N. Benameur, C. Guizard, M. Nygren, Scripta Mater. 60 (2009) 164–167.
- [15] B.N. Kim, K. Hiraga, K. Morita, H. Yoshida, T. Miyazaki, Y. Kagawa, Acta Mater. 57 (2009) 1319–1326.
- [16] J.G.J. Peelen, R. Metselaar, J. Appl. Phys. 45 (1974) 216–220.
- [17] W. Li, L. Gao, J. Eur. Ceram. Soc. 20 (2000) 2441–2445.
- [18] U. Anselmi-Tamburini, J.E. Garay, Z.A. Munir, A. Tacca, F. Maglia, G. Spinolo, J. Mater. Res. 19 (2004) 3255–3262.
- [19] U. Anselmi-Tamburini, J.E. Garay, Z.A. Munir, Scripta Mater. 54 (2006) 823–828.
- [20] J. Reis, R. Chaim, Mater. Sci. Eng. A 491 (2008) 356–363.
- [21] T.O. Saetre, N. Ryum, O. Hunderi, Mater. Sci. Eng. A 108 (1989) 33–36.
- [22] R. Dannenberg, E. Stach, J.R. Groza, J. Mater. Res. 16 (2001) 1090–1095.
- [23] R. Chaim, J. Mater. Res. 12 (1997) 1828–1836.
- [24] O. Hunderi, N. Ryum, Acta Metall. Mater. 29 (1981) 1737–1745.
- [25] R.J. Brook, J. Am. Ceram. Soc. 52 (1969) 56–57.
- [26] L.S. Shvindlerman, G. Gottstein, Scripta Mater. 54 (2006) 1041–1045.
- [27] V. Yu. Novikov, Mater. Lett. 62 (2008) 2067–2069.
- [28] G. Gottstein, L.S. Shvindlerman, Scripta Mater. 54 (2006) 1065–1070.
- [29] A.H. Chokshi, Scripta Mater. 59 (2008) 726–729.
- [30] C.H. Shek, J.K.L. Lai, G.M. Lin, Nanostruct. Mater. 11 (1999) 887–893.
- [31] T.R. Malow, C.C. Koch, Acta Mater. 45 (1997) 2177–2186.
- [32] F. Zhou, J. Lee, E.J. Lavernia, Scripta Mater. 44 (2001) 2013–2017.
- [33] B. Zuo, T. Sritharan, Acta Mater. 53 (2005) 1233–1239.
- [34] F. Ebrahimi, H. Li, Scripta Mater. 55 (2006) 263–266.
- [35] X. Song, J. Zhang, L. Li, K. Yang, G. Liu, Acta Mater. 54 (2006) 5541–5550.
- [36] P. Merkert, H. Hahn, J. Rodel, Nanostruct. Mater. 12 (1999) 701–704.
- [37] I.W. Chen, X.H. Wang, Nature 404 (2000) 168–171.

- [38] H. Yoshida, K. Morita, B.N. Kim, K. Hiraga, M. Kodo, K. Soga, T. Yamamoto, J. Am. Ceram. Soc. 91 (2008) 1707–1710.
- [39] R. Chaim, A. Shlayer, C. Estournes, J. Eur. Ceram. Soc. 29 (2009) 91–98.
- [40] T. Rouxel, D. Murat, J.L. Besson, M. Boncoeur, Acta Mater. 44 (1996) 263–278.
- [41] A. Gallardo-Lopez, A. Dominguez-Rodriguez (private communication).
- [42] Z. Huang, X. Sun, Z. Xiu, S. Chen, C.T. Tsai, Mater. Lett. 58 (2004) 2137–2142.
- [43] R. Raj, F.F. Lange, Acta Metall. 33 (1985) 699–703.
- [44] T. Ikegami, J.G. Li, T. Mori, Y. Moriyoshi, J. Am. Ceram. Soc. 85 (2002) 1725–1729.
- [45] P. Zhang, A. Navrotsky, B. Guo, I. Kennedy, A.N. Clark, C. Leshner, Q. Liu, J. Phys. Chem. C 112 (2008) 932–938.
- [46] X.H. Wang, P.L. Chen, I.W. Chen, J. Am. Ceram. Soc. 89 (2006) 431–437.
- [47] K.E. Harris, V.V. Singh, A.H. King, Acta Mater. 46 (1998) 2623–2633.
- [48] J.W. Cahn, J.E. Taylor, Acta Mater. 52 (2004) 4887–4898.
- [49] W.D. Kingery, B. Francois, in: G.C. Kuczynski, N.A. Hooton, C.F. Gibbon (Eds.), Sintering and Related Phenomena, Gordon and Breach Science Publisher, New York, 1967, pp. 471–498.
- [50] Y. Estrin, G. Gottstein, L.S. Shvindlerman, Acta Mater. 47 (1999) 3541–3549.
- [51] M.N. Rahaman, Ceramic Processing and Sintering, Marcel Dekker, Inc., New York, 2003, p. 600.
- [52] R.G. Munro, Elastic Moduli Data for Polycrystalline Ceramics, NISTIR 6853, NIST structural ceramics database, SRD database no. 30 (2002).
- [53] C.A. Handwerker, R.M. Cannon, R.L. Coble, in: W.D. Kingery (Ed.), Advances in Ceramics, vol. 10, The ACerS Inc., Columbus, 1984, pp. 619–643.
- [54] G.N. Hassold, I.W. Chen, D.J. Srolovitz, J. Am. Ceram. Soc. 73 (1990) 2857–2864.
- [55] V. Tikare, M. Braginsky, E.A. Olevsky, J. Am. Ceram. Soc. 86 (2003) 49–53.
- [56] M.F. Berard, D.R. Wilder, J. Appl. Phys. 34 (1963) 2318–2321.
- [57] M.F. Berard, D.R. Wilder, J. Amer. Ceram. Soc. 52 (1969) 85–88.
- [58] I.W. Chen, G.N. Hassold, D.J. Srolovitz, J. Am. Ceram. Soc. 73 (1990) 2865–2872.
- [59] Y. Estrin, G. Gottstein, L.S. Shvindlerman, Scripta Mater. 41 (1999) 385–390.
- [60] Y. Estrin, G. Gottstein, E. Rabkin, L.S. Shvindlerman, Scripta Mater. 43 (2000) 141–147.
- [61] C.E. Krill III, L. Helfen, D. Michels, H. Natter, A. Fitch, O. Masson, R. Birringer, Phys. Rev. Lett. 86 (2001) 842–845.
- [62] R.L. Coble, J. Appl. Phys. 32 (1961) 787–792.
- [63] R.L. Coble, J. Appl. Phys. 41 (1970) 4798–4807.
- [64] S.J.L. Kang, Y.I. Jung, Acta Mater. 52 (2004) 4573–4578.
- [65] F.M.A. Carpay, J. Am. Ceram. Soc. 60 (1977) 82–83.
- [66] C.H. Hsueh, A.G. Evans, R.L. Coble, Acta Metall. 30 (1982) 1269–1279.
- [67] J. Rodel, A.M. Glaeser, J. Am. Ceram. Soc. 73 (1990) 3302–3312.
- [68] F. Wakai, T. Akatsu, Y. Shinoda, Acta Mater. 54 (2006) 793–805.
- [69] M.N. Rahaman, Ceramic Processing and Sintering, Marcel Dekker, Inc., New York, 2003, p. 577.
- [70] J.E. Hilliard, in: H. Elias (Ed.), Stereology, Springer, Berlin, 1967, pp. 211–215.